Supplementary Information for "Global Surface Winds and Aeolian Sediment Pathways on Mars from the Morphology of Barchan Dunes"

L. Rubanenko[1,2], A. Gunn[1,3], S. Pérez-López[1], L.K. Fenton[4], R.C. Ewing[5], Alejandro Soto[6] and M.G.A Lapôtre[1]

[1] Department of Earth & Planetary Sciences, Stanford University, Stanford, California, USA.

[2] Civil and Environmental Engineering, Technion, Haifa, Israel.

[3] School of Earth, Atmosphere & Environment, Monash University, Clayton, Australia.

[4] Carl Sagan Center, SETI Institute, Mountain View, California, USA.

[5] Department of Geology & Geophysics, Texas A&M, College Station, Texas, USA.

[6] Southwest research Institute, Boulder, Colorado, USA.

1. Filtering Process of Barchan Dune's Outlined by the Neural Network

To increase the robustness of our compilation, we filtered our dataset as follows:

(1) Between 70°S-70°N, we only used images of areas previously mapped as dune fields (Fenton, 2020; Hayward et al., 2012). This was done to save computation time – since our goal is not to detect new barchan dunes on Mars but to characterize migration directions of dunes on Mars on a global scale.

(2) Because barchans tend to occur in fields rather than as solitary landforms, we discarded images (800x800 pixels; 4x4 km) containing less than three objects to remove potentially spurious detections.

(3) Upon manually inspecting our results, we found that the model misclassified some dark sublimation-driven features at southern polar latitudes, such as Dalmatian spots and spiders (Zuber, 2003), as barchans. Consequently, we elected to discard dunes in latitudes poleward of 70°S.

(4) By removing dunes with detection-confidence levels outputted by the detection algorithm lower than 70%, and dunes with convexity defects smaller than 2.5% of total dune length (length + mean horn length). The latter step removed many isolated objects erroneously identified as dunes, but also isolated dome dunes, which are excluded from this study. Our choice of 70% confidence is based on trial and error and visual inspection of the detected objects.

2. Validating Methodology with Manual and In-Situ Measurements on Earth

We validate our approach of determining the dominant wind direction by comparing the migration direction of terrestrial dunes computed from images of terrestrial dunes with independent, direct measurements of sand flux (Figure S1). The average migration direction of all the dunes in the scene agrees with the sand flux measured in the same area.

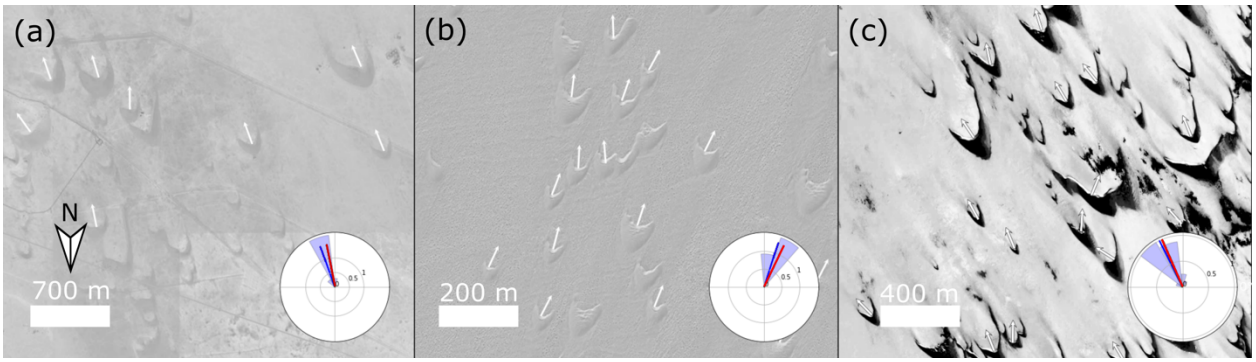

Figure S1: Average barchan migration directions computed from images (blue dial) and direct measurements of sand flux (red dial) in (a) Qatar (25.04°N, 51.40°E): sand flux measured 30 km east of the dune field (b) Sahara (27.7°N, -12.98°E): sand flux measured 26 km west from the dune field (Elbelrhiti et al., 2008) (c) Chad (16.68°N, 17.88°E): sand flux measured 50 km east of the dune field (Baird et al., 2019).

3. Wind-Direction Constraints on Mars from Ground Observations

To further compare with our derived map of global barchan-migration direction (Figure 2), we compiled in-situ measurements wind directions or available proxies on Mars (yellow arrows in Figure 2a):

(1) Viking Lander 1: average 20-sol composite values of wind measurements taken at local lander times 0240, 0701, and 1122 (Hess et al., 1977)
(2) Mars Pathfinder: average orientation of bright wind streaks imaged by the lander and rover (Greeley et al., 1999).
(3) Spirit & Opportunity: wind tail, facet, and groove orientations images by Pancam, Navcam, and Hazcam (Greeley et al., 2008; Sullivan et al., 2005).
(4) Phoenix: anemometer readings collected over the course of 150 sols, weighted by sand flux (Holstein-Rathlou et al., 2010)
(5) Curiosity: ripple migration vectors measured by Mastcam and Mars Descent Imager (MARDI) (Baker et al., 2018; Viúdez-Moreiras et al., 2019)
(6) Insight: TWINS (temperature and wind for Insight) readings were used to compute the wind direction, weighted by wind speeds, computed on three distinct sols (Ls = 13°, 307° and 324°) (Banfield et al., 2020).
(7) Jezero: wind streaks orientations near the Perseverance landing site, derived from HiRISE images (Day & Dorn, 2019; Newman et al., 2022).

4. Global Sand Flux Predictions by the MarsWRF Climate Model

In addition to predictions of global sand flux on Mars by the LMD MCD (Figure 2), we compare our derived migration directions with predictions by the Mars Weather and Research Forecasting (MarsWRF) global general circulation model (Richardson et al., 2007; Figure S2). We use the same simulation setup as Rivera-Valentín et al. (2020) and Chevrier et al. (2020). The model was run with a non-prescribed dust scheme, a CO_2 cycle, and a water cycle that included radiatively active water and dust (Lee et al., 2018).

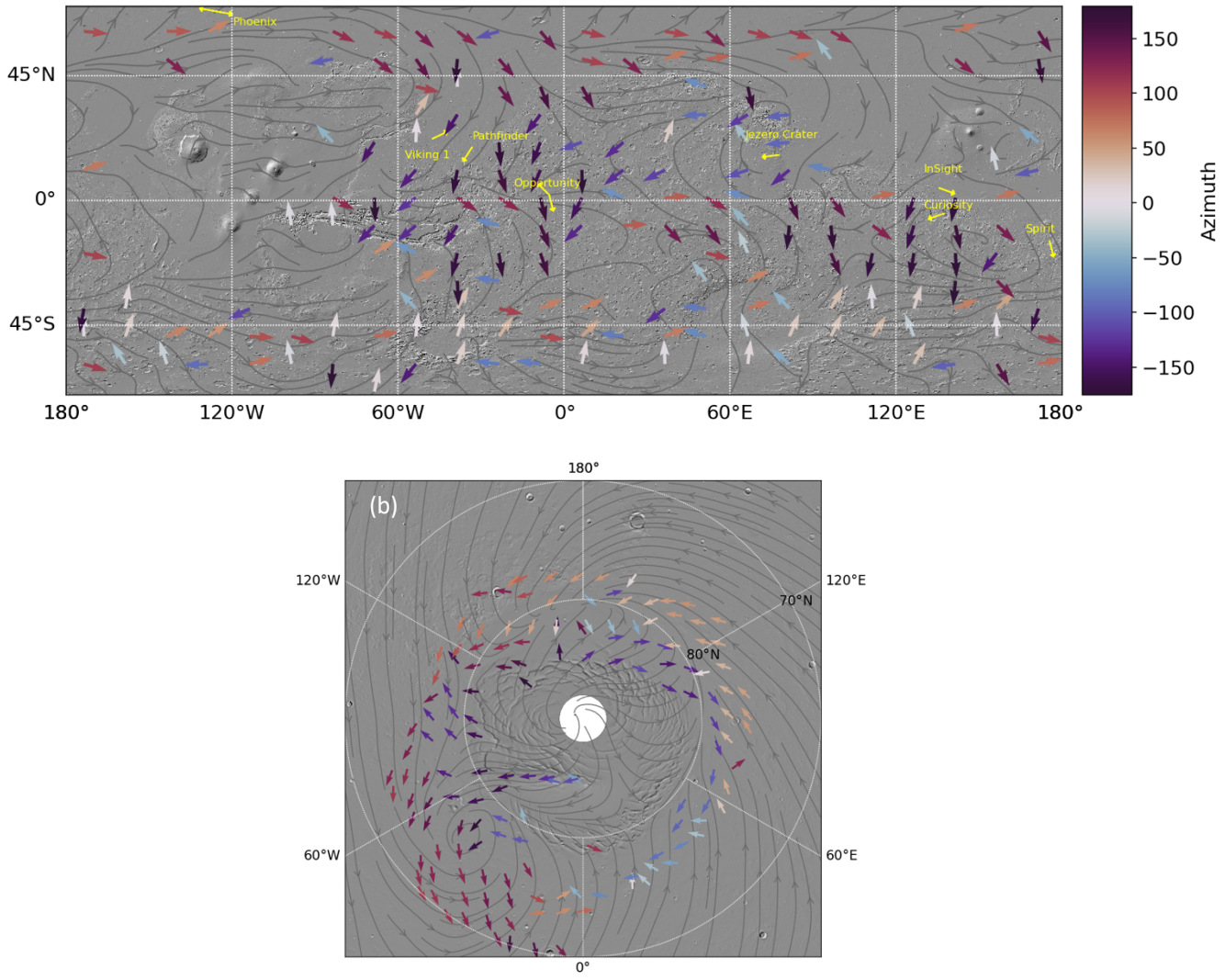

Figure S2: MarsWRF sand flux predictions (gray streamlines) and dune-migration directions (arrows) on Mars. (a) 70S °– 70°N. (b) > 70°N. Yellow arrows with labels indicate local estimates of wind or sand flux direction from landed spacecraft.

5. Comparing Sand Flux Predictions by MarsWRF and LMD GCMs

To compare sand flux predictions by the two GCMs (Figure S3), we compute the angular difference between their predictions the measured migration direction. We find both models provide equally good predications of the migration direction of barchan dunes on Mars. The source of the deviation can be mostly explained by local slopes affecting the global or regional circulation (see discussion in main text).

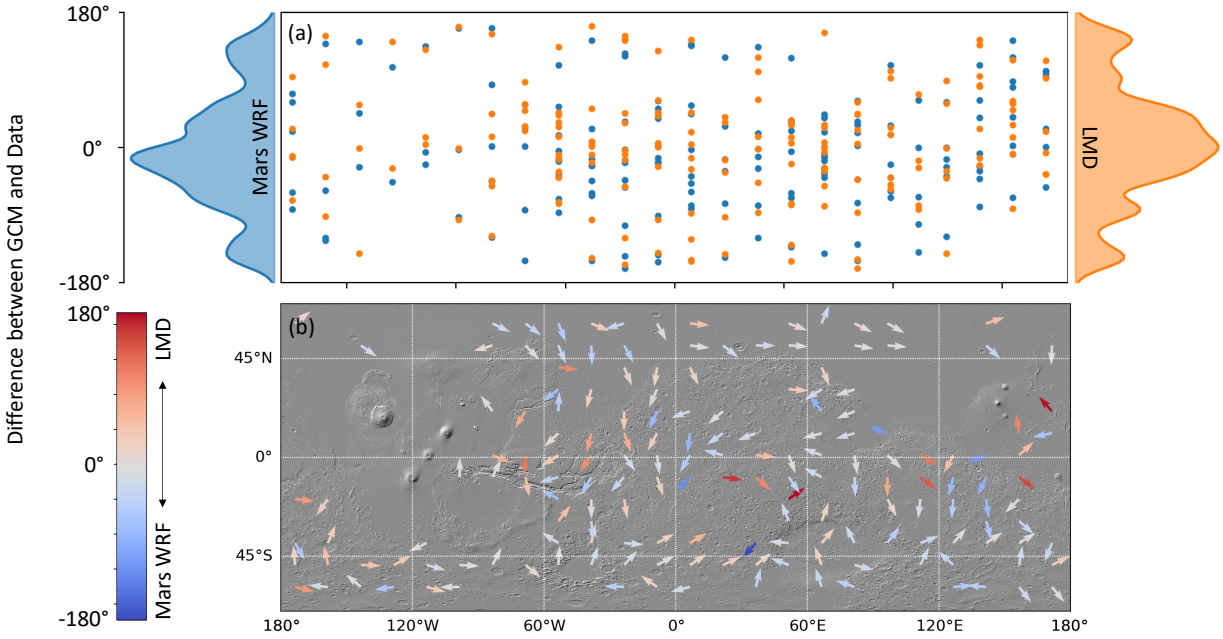

Figure S3: Comparison between the predictions of the two GCMs (LMD and MarsWRF). (a) Angular difference between GCM-predicted sand flux and dune-migration directions, sorted by longitude (horizontal axis). Marginal histograms show the performance of each model. (b) Migration directions of barchan dunes across Mars. Colors indicate the difference in dune-data/model discrepancies between the two models. Blue arrows reflect locations where MarsWRF is in better agreement with barchan-dune migration directions, whereas red arrows indicate locations where the LMD model performs better.

6. Bedform reconstitution timescale

To assess the duration over which barchan-dune morphology and orientation integrate over on Mars, we calculated the bedform reconstitution timescale (e.g., Bagnold, 1942) from compiled dune morphometrics. The reconstitution timescale is the time it takes for a barchan dune to migrate one wavelength and is a good approximation for the time it would take to orient itself with the net above-threshold wind direction. It is calculated as $T_R = L/c$, where dune length L (m) is found as defined in Rubanenko et al., 2022 and migration rate, c (m/s), is the speed the barchan slipface advances in the orientation direction.

Predicted migration rate, c_p, is calculated by pairing the LMD GCM predicted sand flux and dune geometry height, H, from Rubanenko et al., 2022, then calibrated to measured slipface advancing rates measured by Bridges et al. (2012) and Chojnacki et al. (2019) at Nili Patera. Slipface migration, c_p, is defined as $c_p = q/(H\phi\rho_s)$, where q (kg/m/s) is the sediment flux, ϕ is the packing fraction, and ρ_s (kg/m^3) is the sediment density. We assume typical global values for $\phi = 0.7$ and $\rho_s = 3000$ kg/m^3.

Sediment flux, q, is estimated in three steps. First, the net saturated flux vector from the LMD GCM, $\overrightarrow{q_s}$ (kg/m/s), is calculated from the 10-m wind vectors using the Martin & Kok (2017) flux law, as described elsewhere in the text. Second, this flux vector is projected onto the dune migration direction, θ_d, such that the flux in the saturated flux in dune direction, $q_{s,d} = |\overrightarrow{q_s}||\cos(\angle\overrightarrow{q_s} - \theta_d)|$. Third, the saturated flux in the dune direction is scaled to the true flux the barchan experiences, q, which is the average stoss flux. The average stoss flux is the average of the flux at the toe (which is zero since we are only considering isolated barchans) and the flux at the brink, q_b, which is higher than the saturated flux due to the wind speed-up effect over the positive stoss slope. Thus, $q = q_b/2$. The brink flux is calculated as $q_b = q_{s,d}(1 + \beta s)$, where β is a dimensionless speed-up factor of ~9.44 for dunes (Gunn, 2022), and s is the stoss slope $s = H/(L - H/\tan\theta_{sf})$, where $\theta_{sf} = 30°$ is the slipface angle.

Predictions of dune migration rate, c, made as described above from LMD GCM outputs, chosen flux law, and barchan geometries are smaller than observed martian dune migration rates measured using repeat HiRISE images by Chojnacki et al. (2019) and Bridges et al. (2012). This discrepancy is to be expected for a variety of reasons, including potential misrepresentation of near-surface winds in the GCM as demonstrated by other results in the paper, and the fact that flux laws have not been directly calibrated to saltation on Mars. We do believe, however, that despite the error in absolute values in migration speeds, the spatial pattern in relative migration speeds is relatively robust (Fig. S4a). This is because while the Earth-calibrated prefactor from the Martin & Kok (2014) flux law may not hold on Mars, the exponent in the flux relationship should be more reliable. As a result, we can empirically calibrate c as $c = c_p c_{NP,m}/c_{NP,p}$, where $c_{NP,m}$ is the mean of measured dune migration speeds, c_m, at Nili Patera ($c_{NP,m} \approx 0.769$ m/Earth year or m/EY as estimated by Chojnacki et al., 2019, or 0.562 m/EY as estimated by Bridges et al., 2012). This recalibration still does not include the effect of surface volatiles, where seasonal frost away from the equator may affect the calculated migration rates, and hence, T_R.

Finally, the probability distribution of calculated T_R values are given as $T_R = L/c$ in Fig. S4b. The mode of this distribution is approximately 100 Mars years (MY), with a range from 10 to 10^4 MY. In comparison Mars' obliquity, eccentricity, and precession display periods of ~64×10^3, 50×10^3, and ~27×10^3 MY, with additional periods that exceed 10^6 EY (Schorghofer, 2008). Such short reconstitution timescales confirm that derived dune migration directions reflect the modern wind circulation of Mars rather than past conditions (Fenton & Richardson, 2001). We emphasize again that these short restitution timescales only reflect those of isolated barchan dunes; larger dunes would have longer reconstitution timescales, and in turn, may record information about recent atmospheric change on Mars (Ewing et al., 2010).

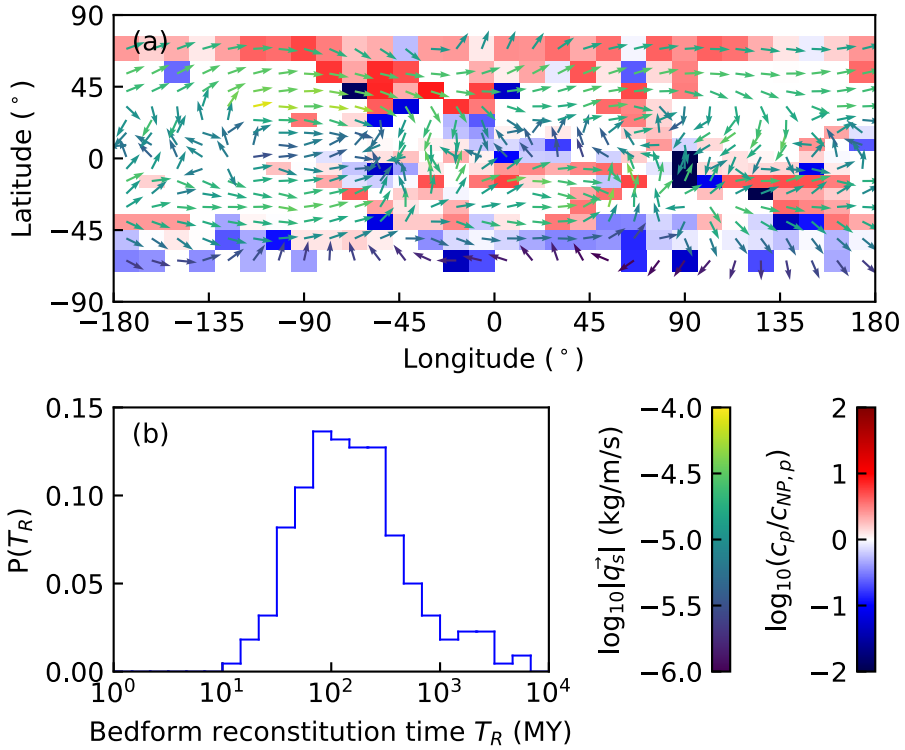

Figure S4. (a) Map of mars colored by the logarithm of the predicted dune migration speeds, c_p (m/s), normalised by the predicted dune migration speed at Nili Patera, $c_{NP,p}$ (m/s), overlaid by the saturated flux vector directions colored by the logarithm of the flux vector magnitudes predicted by the LMD GCM. (b) The global probability distribution of the predicted bedform reconstitution times, T_R (MY).

References:

Bagnold, R. A. (1942). *The physics of blown sand and desert dunes*. New York, W. Morrow & company.

Baird, T., Bristow, C. S., & Vermeesch, P. (2019). Measuring sand dune migration rates with COSI-Corr and landsat: Opportunities and challenges. *Remote Sensing*, *11*(20), 2423.

Baker, M. M., Lapôtre, M. G. A., Minitti, M. E., Newman, C. E., Sullivan, R., Weitz, C. M., et al. (2018). The Bagnold Dunes in southern summer: Active sediment transport on Mars observed by the Curiosity rover. *Geophysical Research Letters*, *45*(17), 8853–8863.

Banfield, D., Spiga, A., Newman, C., Forget, F., Lemmon, M., Lorenz, R., et al. (2020). The atmosphere of Mars as observed by InSight. *Nature Geoscience*, *13*(3), 190–198.

Bridges, N. T., Bourke, M. C., Geissler, P. E., Banks, M. E., Colon, C., Diniega, S., et al. (2012). Planet-wide sand motion on Mars. *Geology*, *40*(1), 31–34.

Chevrier, V. F., Rivera-Valentín, E. G., Soto, A., & Altheide, T. S. (2020). Global temporal and geographic stability of brines on present-day Mars. *The Planetary Science Journal*, *1*(3), 64.

Chojnacki, M., Banks, M. E., Fenton, L. K., & Urso, A. C. (2019). Boundary condition controls on the high-sand-flux regions of Mars. *Geology*, *47*(5), 427–430.

Day, M., & Dorn, T. (2019). Wind in Jezero crater, Mars. *Geophysical Research Letters*, *46*(6), 3099–3107.

Elbelrhiti, H., Andreotti, B., & Claudin, P. (2008). Barchan dune corridors: field characterization and investigation of control parameters. *JGR: Earth Surface*, *113*(F2).

Ewing, R. C., Peyret, A. B., Kocurek, G., & Bourke, M. (2010). Dune field pattern formation and recent transporting winds in the Olympia Undae Dune Field, north polar region of Mars. *Journal of Geophysical Research: Planets*, *115*(E8).

Fenton, L. K. (2020). Updating the global inventory of dune fields on Mars and identification of many small dune fields. *Icarus*, *352*, 114018.

Fenton, L. K., & Richardson, M. I. (2001). Martian surface winds: Insensitivity to orbital changes and implications for aeolian processes. *Journal of Geophysical Research: Planets*, *106*(E12), 32885–32902.

Greeley, R., Kraft, M., Sullivan, R., Wilson, G., Bridges, N., Herkenhoff, K., et al. (1999). Aeolian features and processes at the Mars Pathfinder landing site. *JGR: Planets*, *104*(E4), 8573–8584.

Greeley, R., Whelley, P. L., Neakrase, L. D. V, Arvidson, R. E., Bridges, N. T., Cabrol, N. A., et al. (2008). Columbia Hills, Mars: Aeolian features seen from the ground and orbit. *JGR: Planets*, *113*(E6).

Hayward, R. K., Fenton, L. K., Titus, T. N., Colaprete, A., & Christensen, P. R. (2012). Mars global digital dune database: MC-30. *US Geological Survey Open-File Report*, *1259*.

Hess, S. L., Henry, R. M., Leovy, C. B., Ryan, J. A., & Tillman, J. E. (1977). Meteorological results from the surface of Mars: Viking 1 and 2. *JGR*, *82*(28), 4559–4574.

Holstein-Rathlou, C., Gunnlaugsson, H. P., Merrison, J. P., Bean, K. M., Cantor, B. A., Davis, J. A., et al.

(2010). Winds at the Phoenix landing site. *JGR: Planets*, *115*(E5).

Lee, C., Richardson, M. I., Newman, C. E., & Mischna, M. A. (2018). The sensitivity of solsticial pauses to atmospheric ice and dust in the MarsWRF General Circulation Model. *Icarus*, *311*, 23–34.

Martin, R. L., & Kok, J. F. (2017). Wind-invariant saltation heights imply linear scaling of aeolian saltation flux with shear stress. *Science Advances*, *3*(6), e1602569.

Newman, C. E., Hueso, R., Lemmon, M. T., Munguira, A., Vicente-Retortillo, Á., Apestigue, V., et al. (2022). The dynamic atmospheric and aeolian environment of Jezero crater, Mars. *Science Advances*, *8*(21), eabn3783.

Richardson, M. I., Toigo, A. D., & Newman, C. E. (2007). PlanetWRF: A general purpose, local to global numerical model for planetary atmospheric and climate dynamics. *JGR: Planets*, *112*(E9).

Rivera-Valentín, E. G., Chevrier, V. F., Soto, A., & Martínez, G. (2020). Distribution and habitability of (meta) stable brines on present-day Mars. *Nature Astronomy*, *4*(8), 756–761.

Rubanenko, L., Lapotre, M. G. A., Ewing, R. C., Fenton, L. K., & Gunn, A. (2022). A distinct ripple-formation regime on Mars revealed by the morphometrics of barchan dunes. *Nature Communications*.

Schorghofer, N. (2008). Temperature response of Mars to Milankovitch cycles. *Geophysical Research Letters*, *35*(18).

Sullivan, R., Banfield, D., Bell, J. F., Calvin, W., Fike, D., Golombek, M., et al. (2005). Aeolian processes at the Mars exploration rover Meridiani Planum landing site. *Nature*, *436*(7047), 58–61.

Viúdez-Moreiras, D., Gómez-Elvira, J., Newman, C. E., Navarro, S., Marin, M., Torres, J., & De La Torre-Juárez, M. (2019). Gale surface wind characterization based on the Mars Science Laboratory REMS dataset. Part I: Wind retrieval and Gale's wind speeds and directions. *Icarus*, *319*, 909–925.

Zuber, M. T. (2003). Learning to think like martians. *Science*, *302*(5651), 1694–1695.